Simulating Magnetic Nanoparticle Behavior in Low-field MRI under Transverse Rotating Fields and Imposed Fluid Flow

P. Cantillon-Murphy[a,b], **L.L. Wald**[c], **E. Adalsteinsson**[b,c], and **M. Zahn**[b]

P. Cantillon-Murphy: padraig@mit.edu; L.L. Wald: wald@nmr.mgh.harvard.edu; E. Adalsteinsson: elfar@mit.edu; M. Zahn: zahn@mit.edu

[a] Department of Gastroenterology, Brigham and Women's Hospital, Boston, MA

[b] Department of Electrical Engineering and Computer Science, Massachusetts Institute of Technology, Cambridge, MA

[c] MGH-HST Athinoula A. Martinos Center for Biomedical Imaging, Charlestown, MA

Abstract

In the presence of alternating-sinusoidal or rotating magnetic fields, magnetic nanoparticles will act to realign their magnetic moment with the applied magnetic field. The realignment is characterized by the nanoparticle's time constant, τ. As the magnetic field frequency is increased, the nanoparticle's magnetic moment lags the applied magnetic field at a constant angle for a given frequency, Ω, in rad/s. Associated with this misalignment is a power dissipation that increases the bulk magnetic fluid's temperature which has been utilized as a method of magnetic nanoparticle hyperthermia, particularly suited for cancer in low-perfusion tissue (e.g., breast) where temperature increases of between 4°C and 7°C above the ambient *in vivo* temperature cause tumor hyperthermia. This work examines the rise in the magnetic fluid's temperature in the MRI environment which is characterized by a large DC field, B_0. Theoretical analysis and simulation is used to predict the effect of both alternating-sinusoidal and rotating magnetic fields transverse to B_0. Results are presented for the expected temperature increase in small tumors (~1 cm radius) over an appropriate range of magnetic fluid concentrations (0.002 to 0.01 solid volume fraction) and nanoparticle radii (1 to 10 nm). The results indicate that significant heating can take place, even in low-field MRI systems where magnetic fluid saturation is not significant, with careful The goal of this work is to examine, by means of analysis and simulation, the concept of interactive fluid magnetization using the dynamic behavior of superparamagnetic iron oxide nanoparticle suspensions in the MRI environment. In addition to the usual magnetic fields associated with MRI, a rotating magnetic field is applied transverse to the main B_0 field of the MRI. Additional or modified magnetic fields have been previously proposed for hyperthermia and targeted drug delivery within MRI. Analytical predictions and numerical simulations of the transverse rotating magnetic field in the presence of B_0 are investigated to demonstrate the effect of Ω, the rotating field frequency, and the magnetic field amplitude on the fluid suspension magnetization. The transverse magnetization due to the rotating transverse field shows strong dependence on the characteristic time constant of the fluid suspension, τ. The analysis shows that as the rotating field frequency increases so that $\Omega\tau$ approaches unity, the transverse fluid magnetization vector is significantly non-aligned with the applied rotating field and the magnetization's magnitude is a strong function of the field frequency. In this frequency range, the fluid's transverse magnetization is controlled by the applied field which is determined by the operator.

The phenomenon, which is due to the physical rotation of the magnetic nanoparticles in the suspension, is demonstrated analytically when the nanoparticles are present in high concentrations (1 to 3% solid volume fractions) more typical of hyperthermia rather than in clinical imaging applications, and in low MRI field strengths (such as open MRI systems), where the magnetic nanoparticles are not magnetically saturated. The effect of imposed Poiseuille flow in a planar channel geometry and changing nanoparticle concentration is examined. The work represents the first known attempt to analyze the dynamic behavior of magnetic nanoparticles in the MRI environment including the effects of the magnetic nanoparticle spin-velocity. It is shown that the magnitude of the transverse magnetization is a strong function of the rotating transverse field frequency. Interactive fluid magnetization effects are predicted due to non-uniform fluid magnetization in planar Poiseuille flow with high nanoparticle concentrations.

Keywords

Magnetic nanoparticles; MRI; rotating magnetic field; interactive magnetization; magnetic particle imaging

1 Introduction

The ferrohydrodynamics of suspensions of superparamagnetic iron-oxide (most usually magnetite-dominated) in carrier liquids such as oil or water, commonly termed ferrofluids, is well-understood [1–4]. Following the analysis of Shliomis, [1], much work has sought to validate his theory through experiments [5–7]. With the work of Weissleder [8] among others [9], [10], water-based ferrofluids have found application as imaging contrast agents in magnetic resonance imaging (MRI), where they are known as superparamagnetic iron oxide (SPIO) contrast agents. More recently, magnetic nanoparticles have received much attention as the heat source in magnetic particle hyperthermia (MPH) [11] and as a mechanism for targeted drug delivery *in vivo* [12]. Also, modifications and additions to the existing MRI gradient fields have been proposed as a method for targeted particle delivery [12,13]. Most recently, an alternate imaging modality to MRI known as magnetic particle imaging (MPI) [14] has been proposed which uses the non-linear magnetic response of magnetic nanoparticles (*i.e.*, the Langevin relation) for direct imaging of their distribution. While much important work has been undertaken to characterize the biomedical, physical and non-dynamic magnetic properties of such SPIO-type agents [15], [16], including the relaxivity critical to contrast in MRI [17–20], there has yet been no attempt to analyze the potential effect of nanoparticle dynamics within MRI. This work represents a preliminary investigation of the dynamic behavior by means of analysis and numerical simulations. Potential application of the described phenomena for interactive fluid magnetization is outlined, including a proposed experimental investigation of the effect. Similarities between the physical characteristics of the nanoparticles investigated in this work with other biomedical applications of magnetic nanoparticles are also noted, including those applicable to MPH and targeted drug delivery systems.

Fundamental to conventional MRI are three applied magnetic flux densities: a strong, homogenous *z*-directed DC field, B_0; a transverse RF field, $\boldsymbol{B_1}$; and spatially-varying encoding fields or gradients, $\boldsymbol{G}$, also *z*-directed. The B_0-field (~1.5 T) induces polarization of nuclear spins, the much weaker (~0.01 mT) and transient (~ms) $\boldsymbol{B_1}$ field is used to drive the induced magnetization into a transverse component for imaging, and the gradients (~10 mT/m) are used to spatially encode the transverse magnetization during relaxation to a resting state (~10 ms). Under the large B_0 of conventional clinical MRI systems, it is expected that the equilibrium magnetization of a water-based ferrofluid would be saturated and virtually all the magnetic particles in the suspension would rigidly align with B_0. However, low-field MRI platforms exist, typically employed for better patient access or intervention by physicians during

scanning. Commercial low-field MRI scanners operate typically between 0.1 T and 0.35 T, and this is the field-range examined in the simulations which follow. With this lower B_0, ferrofluid saturation is not complete, as determined by the Langevin relation for magnetic suspensions [2]. Physical nanoparticle rotation in an additional rotating magnetic field is therefore possible. In our analysis, we derive the expression for the ferrofluid spin velocity, ω, induced by imposing a fourth field component, $\boldsymbol{B}_e$, to a conventional MRI. Although not easily measureable, ω is used in this work as a quantifiable analytical indication of the non-alignment between the field exciting the ferrofluid, $\boldsymbol{B}_e$, which is a rotating field applied in the transverse xy plane, and the associated transverse magnetization vector. While both $\boldsymbol{B}_e$ and $\boldsymbol{B}_1$ are transverse, rotating fields, f_0, the rotation frequency of $\boldsymbol{B}_1$, known as the Larmor frequency, is proportional to B_0 as given by (1), where γ is the gyromagnetic ratio of the nucleus under study, which for conventional MRI is the ^{1}H proton with $\gamma = 2\pi \cdot 42.58 \times 10^6$ rad $\cdot$ (T $\cdot$ s)$^{-1}$.

$$f_0 = \frac{\gamma}{2\pi} B_0$$

(1)

This work examines a wide range of rotation frequencies for $\boldsymbol{B}_e$ including those typical of f_0 in open MRI systems (where the Larmor frequency is 8.5 MHz for 0.2 T and 14.9 MHz for 0.35 T). However, the amplitude of $\boldsymbol{B}_e$ is set between 1% and 10% of B_0, which is much larger than typical $\boldsymbol{B}_1$ amplitudes although it is of the same order as fields proposed in MPH [11]. Interactions with the transverse magnetization is achieved by selecting the transverse $\boldsymbol{B}_e$ excitation frequency, termed Ω, to be of the same order as the reciprocal of the ferrofluid relaxation time τ. For typical magnetic nanoparticles in biomedical applications, τ is on the order of 1 μs.

A simple but important channel geometry introduced by Zahn and Greer [21] shown in Fig. 1 is analyzed, which allows imposition of boundary conditions on both magnetic fields and fluid flow. A novel linearization of the Langevin relation for magnetic fluid suspensions is presented for small signal field variations around the operating point determined by the B_0 field. Having established this linearization, the scenario of a concurrent B_0 and transverse rotating $\boldsymbol{B}_e$ field is examined for the case of Poiseuille flow [22] where fluid flow is due to a pressure differential along the channel length. Two critical parameters of interest are examined. These are the ferrofluid spin-velocity in the channel and the resultant change in the transverse ferrofluid magnetization that arises due to the simultaneous relaxation and realignment of the magnetic nanoparticles with the applied transverse rotating field. Results for both quantities are examined for magnetic nanoparticles with physical characteristics typical of magnetic nanoparticle contrast agents used in MRI as well as those proposed for magnetic nanoparticle hyperthermia and targeted drug delivery.

2 Theory

2.1 Linearization of the Langevin Relation

The Langevin relation relates the ratio of the magnetic and thermal energy densities in a ferrofluid [2]. It takes the form of (2) and $L(\alpha)$ describes the degree of alignment of the ferrofluid magnetic nanoparticles with the applied magnetic field, of magnitude $|\boldsymbol{H}|$. The Langevin parameter, α, is a function of the magnetic field magnitude, $|\boldsymbol{H}|$, within the ferrofluid, as given by (3) where M_d is the single domain magnetization of the particle (typically with a value of 446 kA/m for magnetite [2]), V_p is the particle magnetic volume, μ_0 is the magnetic permeability of free space, k is Boltzmann's constant and T is the absolute temperature. The

ferrofluid saturation magnetization M_s is related to M_d by the fraction of solid magnetic volume in the suspension, denoted φ where $M_s = \varphi M_d$.

$$M_{eq}=M_s L(\alpha)=M_s(\coth(\alpha) - 1/\alpha) \tag{2}$$

$$\alpha=\frac{M_d V_p \mu_0 |\boldsymbol{H}|}{kT} \tag{3}$$

Linearization of the Langevin function can be performed about a DC operating point defined by the magnetic field intensity, H_0. In this work, H_0 represents the large DC magnetic field which characterizes MRI. It is assumed that there are no large-signal DC components directed along $\boldsymbol{i}_x$ or $\boldsymbol{i}_y$ which are unit vectors along the x and y axes respectively so that H_0 is directed along $\boldsymbol{i}_z$, the unit vector along z. Additional small-signal perturbations about that operating point along $\boldsymbol{i}_x$, $\boldsymbol{i}_y$ and $\boldsymbol{i}_z$ are denoted by h_x, h_y and h_z respectively leading to the expression in (4).

$$\boldsymbol{H}=h_x \boldsymbol{i}_x+h_y \boldsymbol{i}_y+(H_0+h_z)\boldsymbol{i}_z \tag{4}$$

The associated total equilibrium ferrofluid magnetization vector is $\boldsymbol{M}_{eq}$ where the components of magnetization due to the perturbations along $\boldsymbol{i}_x$, $\boldsymbol{i}_y$ and $\boldsymbol{i}_z$ are denoted m_x, m_y and m_z respectively.

$$\boldsymbol{M}_{eq}=m_x \boldsymbol{i}_x+m_y \boldsymbol{i}_y+(M_0+m_z)\boldsymbol{i}_z \tag{5}$$

Since $\boldsymbol{H}$ and $\boldsymbol{M}_{eq}$ are necessarily collinear, $\boldsymbol{M}_{eq}$ is written in terms of (4).

$$\boldsymbol{M}_{eq}=M_s L(\alpha)\frac{h_x \boldsymbol{i}_x+h_y \boldsymbol{i}_y+(H_0+h_z)\boldsymbol{i}_z}{\sqrt{(h_x)^2+(h_y)^2+(H_0+h_z)^2}} \tag{6}$$

The following analysis considers first-order, linearized small-signal perturbations to the magnetic field components (denoted h_x, h_y, h_z) and the associated small-signal contributions to the magnetization components (m_x, m_y, m_z), added to the large, z-directed equilibrium DC field component, H_0 with associated DC magnetization component along z, denoted M_0. The equilibrium magnetization, given by (2), will be linearized for the imposed small-signal magnetic field perturbations to yield linearized, first-order expressions for m_x, m_y and m_z. The total resultant magnetization associated with the nanoparticle suspension consists of the DC component, M_0, along z, added to the small-signal contributions, m_x, m_y and m_z along x, y and z respectively.

Considering a first-order expansion of the denominator of (6), one can rewrite the expression for $\boldsymbol{M}_{eq}$ as simplified in (7) when all second-order terms (*e.g.*, $h_x h_z$ and $h_y h_z$) are ignored. Note that there is no first order perturbation to the z-directed component of the Langevin magnetization.

$$M_{eq} \approx M_s L(\alpha) \frac{h_x \boldsymbol{i}_x + h_y \boldsymbol{i}_y + (H_0 + h_z)\boldsymbol{i}_z}{H_0}(1 - \frac{h_z}{H_0})$$
$$\approx M_s L(\alpha) \frac{h_x \boldsymbol{i}_x + h_y \boldsymbol{i}_y + (H_0)\boldsymbol{i}_z}{H_0}$$

(7)

The Langevin parameter, α, is written as the linear sum of contributions due to the Langevin function evaluated at the operating point (denoted α_0) and contributions due to the small-signal perturbations (denoted α'). The terms α_0 and α' are evaluated by a first-order expansion of (2) and (3) where $|\boldsymbol{H}|$ is found from (4) to yield (10) and (11).

$$\alpha = \alpha_0 + \alpha'$$

(8)

$$\alpha = \frac{M_d V_p \mu_0}{kT} \sqrt{(h_x)^2 + (h_y)^2 + (H_0 + h_z)^2}$$
$$\approx \frac{M_d V_p \mu_0}{kT} H_0 (1 + \frac{h_z}{H_0})$$

(9)

$$\Rightarrow \alpha_0 = \frac{M_d V_p \mu_0 H_0}{kT}$$

(10)

$$\Rightarrow \alpha' = \alpha_0 \frac{h_z}{H_0}$$

(11)

Simplifying the expression for the Langevin Relation in (12) [2] using a first-order Taylor Series expansion, leads to (14).

$$L(\alpha) = \coth(\alpha_0 + \alpha') - \frac{1}{\alpha_0 + \alpha'}$$

(12)

$$L(\alpha) \approx L(\alpha_0) + \frac{dL(\alpha)}{d\alpha}|_{\alpha = \alpha_0} \alpha'$$

(13)

$$L(\alpha) \approx \coth(\alpha_0) - \frac{1}{\alpha_0} - \frac{\alpha'}{\sinh^2(\alpha_0)} + \frac{\alpha'}{\alpha_0^2}$$

(14)

$$m_x \approx M_s(\coth(\alpha_0) - \frac{1}{\alpha_0} - \frac{\alpha'}{\sinh^2(\alpha_0)} + \frac{\alpha'}{\alpha_0^2})\frac{h_x}{H_0}$$

(15)

$$m_y \approx M_s(\coth(\alpha_0) - \frac{1}{\alpha_0} - \frac{\alpha'}{\sinh^2(\alpha_0)} + \frac{\alpha'}{\alpha_0^2})\frac{h_y}{H_0}$$

(16)

$$M_{eq,z} \approx m_z + M_0 \approx M_s(\coth(\alpha_0) - \frac{1}{\alpha_0} - \frac{\alpha'}{\sinh^2(\alpha_0)} + \frac{\alpha'}{\alpha_0^2})$$

(17)

Substituting for $L(\alpha)$ in (7) (as shown in (15) through (17)) allows the constituent components of $\boldsymbol{M}_{eq}$ to be expressed as follows by comparison with (5) where the component due to the zeroth order DC H_0 field, which is only z-directed, is given by (21). The first-order, small-signal magnetization components, m_x, m_y and m_z, follow from substituting for α' and ignoring second and higher order terms.

$$m_x \approx M_s L(\alpha_0)\frac{h_x}{H_0} \approx \frac{M_0}{H_0}h_x$$

(18)

$$m_y \approx M_s L(\alpha_0)\frac{h_y}{H_0} \approx \frac{M_0}{H_0}h_y$$

(19)

$$m_z \approx M_s(\frac{-\alpha_0}{\sinh^2\alpha_0} + \frac{1}{\alpha_0})\frac{h_z}{H_0} \approx \frac{dM_0}{dH_0}h_z$$

(20)

$$M_0 = M_s L(\alpha_0)$$

(21)

The expressions of (18) through (21) show that for z-directed perturbations, the relationship between the small signal magnetic field and the resultant magnetization is due to the slope of the Langevin relation evaluated at the DC operating point defined by $H_0 = B_0/\mu_0 - M_0$. When the perturbations are either x or y-directed, the small signal magnetic field (h_x and h_y) and the resultant magnetizations (m_x and m_y) are related by the ratio M_0/H_0. Comparing these two relations in Figure 2, it is easily shown that the two relations are approximately equal in the low-field limit where $\alpha_0 \ll 1$ and M_0 is proportional to H_0.

This work examines the case of small-signal magnetic field perturbations along $\boldsymbol{i}_x$ and $\boldsymbol{i}_y$ which are temporally displaced by $\frac{\pi}{2}$ radians, to create a rotating field in the transverse $\{xy\}$ plane. No small-signal perturbations are considered along $\boldsymbol{i}_z$ ($h_z = 0$). The DC field is limited to variations between 0.1 T and 0.35 T in the results which follow since nanoparticles with a magnetic core radius of 4 nm (typical of MRI contrast agents) are already 90% saturated ($L(\alpha_0) \approx 0.9$) at $B_0 = 0.35$ T.

2.2 Governing Equations

The geometry shown in Fig. 1 follows the analysis of Zahn and Greer [21] and is carefully selected to allow the imposition of fields directed along all three axes.

2.2.1 Magnetization Constitutive Law—The magnetization relaxation equation for a ferrofluid under the action of a rotating magnetic field, thereby undergoing simultaneous magnetization and reorientation with the applied field, is given by (22). The fluid linear flow velocity vector is v, the ferrofluid spin-velocity vector is ω and the ferrofluid relaxation time [2] is τ.

$$\frac{\partial M}{\partial t} + v \cdot \nabla M - \omega \times M + (1/\tau)(M - M_{eq}) = 0 \tag{22}$$

The left-side of the relaxation equation is simply a generalized convective derivative of magnetization for linear motion (at linear velocity v) and angular or spin velocity, ω. The equation states that deviations away from the equilibrium magnetization in a magnetic fluid have a characteristic time constant, denoted τ. The time constant, τ, is given by (23) and is due to the contributions from Brownian (τ_B) and Néel (τ_N) relaxation times [2,25].

$$\frac{1}{\tau} = \frac{1}{\tau_B} + \frac{1}{\tau_N} \tag{23}$$

The relative expressions for τ_B and τ_N are given by (24) and (25) respectively where V_h is the nanoparticle hydrodynamic volume in m^3 (including the surfactant contribution), η_c is the dynamic viscosity of the carrier liquid (assumed that of water in this analysis) in $N \cdot s \cdot m^{-2}$, k is Boltzmann's constant ($1.38 \times 10^{-23} \, m^2 \cdot kg \cdot s^{-2} \cdot K^{-1}$), T is the absolute temperature in K (assumed 295 K unless stated), V_p is the nanoparticle volume in m^3 (excluding surfactant contribution), K_a is the anisotropy constant in $J \cdot m^{-3}$ and τ_0 is the characteristic Néel time given by Rosensweig [2] as 1 ns.

$$\tau_B = \frac{3V_h \eta_c}{kT} \tag{24}$$

$$\tau_N = \tau_0 e^{\frac{K_a V_p}{kT}} \tag{25}$$

In (23), the smaller time constant dominates in determining τ. Thus, while both Brownian and Néel relaxation times increase with particle radius [2], Néel relaxation, which describes the rotation of the magnetization vector within the particle, generally dominates for small particles with core radius less than 4 nm while Brownian relaxation, due to particle rotation in the carrier liquid, dominates for particles larger than 4 nm [25]. If the nanoparticle is constrained, for example by attachment to a surface, Néel relaxation is still operative while Brownian relaxation is not.

For the planar geometry shown in Fig. 1, the flow velocity can only be x-directed and the time-averaged spin-velocity can only be z-directed. Both quantities may vary spatially with y.

$$v = v_x(y) i_x \tag{26}$$

$$\omega = \omega_z(y)\boldsymbol{i}_z \qquad (27)$$

2.2.2 Magnetic Fields—Considering the geometric arrangement of Fig. 1, the imposed magnetic field intensities along $\boldsymbol{i}_x$ and $\boldsymbol{i}_z$ are spatially uniform with corresponding zero spatial derivatives. This follows from Ampère's Law, given by (28), which states that in the absence of any conduction ($\boldsymbol{J} = \boldsymbol{0}$) or displacement current densities ($\frac{\partial D}{\partial t} \neq \boldsymbol{0}$), the curl of the magnetic field intensity in the ferrofluid channel is necessarily zero, as given by (28). For the geometry of Fig. 1, this means that both the x and z components of magnetic field intensity are uniform in the channel since H_0 is invariant in space. The convenience of the planar channel should now be apparent where field derivatives with respect to x and z are taken to be zero while the pressure gradient, $\frac{\partial p}{\partial x}$ can remain non-zero, allowing for the imposition of linear flow.

$$\nabla \times \boldsymbol{H} = \boldsymbol{J} + \frac{\partial \boldsymbol{D}}{\partial t} = \boldsymbol{0} \qquad (28)$$

$$
\begin{aligned}
&\Rightarrow \frac{\partial(H_0)}{\partial y} - \frac{\partial h_y}{\partial z} = 0 \quad \Rightarrow \frac{\partial(H_0)}{\partial y} = 0, \ \frac{\partial h_y}{\partial z} = 0 \\
&\Rightarrow \frac{\partial h_x}{\partial z} - \frac{\partial(H_0)}{\partial x} = 0 \quad \Rightarrow \frac{\partial(H_0)}{\partial x} = 0, \ \frac{\partial h_x}{\partial z} = 0, \\
&\quad\ \Rightarrow \frac{\partial h_y}{\partial x} - \frac{\partial h_x}{\partial y} = 0 \Rightarrow \frac{\partial h_y}{\partial x} = 0, \ \frac{\partial h_x}{\partial y} = 0
\end{aligned}
\qquad (29)
$$

The imposed magnetic flux density along $\boldsymbol{i}_y$ is governed by Gauss' Law.

$$\nabla \cdot \boldsymbol{B} = \frac{\partial b_x}{\partial x} + \frac{\partial b_y}{\partial y} + \frac{\partial(B_0)}{\partial z} = 0 \qquad (30)$$

$$\Rightarrow \frac{\partial b_y}{\partial y} = 0 \ \text{ since } \ \frac{\partial b_x}{\partial x} = \frac{\partial(B_0)}{\partial z} = 0 \qquad (31)$$

In light of these observations, it can be seen that b_y and h_x can only be spatially constant, independent of y while h_y may depend on y if there is a y-dependence in m_y. The total instantaneous magnetic flux density, $\boldsymbol{B}$, the total instantaneous magnetic field, $\boldsymbol{H}$, and the total instantaneous magnetization, $\boldsymbol{M}$ are given by (32), (33) and (34) respectively where h_x and h_y are now sinusoidally time-varying quantities and $h_z = 0$. Complex amplitude notation is used for convenience. The $\wedge$ symbol denotes a complex amplitude, $\Re e$ signifies the real component of a complex quantity, Ω is the frequency of excitation in rad·s^{-1} and $j = \sqrt{-1}$. The relationship between $\boldsymbol{B}$, $\boldsymbol{H}$ and $\boldsymbol{M}$ is given by the familiar expression of (35).

$$\boldsymbol{B} = \Re e\{(\widehat{b}_x(y)\boldsymbol{i}_x + \widehat{b}_y\boldsymbol{i}_y)\mathrm{e}^{j\Omega t}\} + B_0\boldsymbol{i}_z \qquad (32)$$

$$H = \Re e\{(\widehat{h}_x i_x + \widehat{h}_y(y) i_y) e^{j\Omega t}\} + H_0 i_z \tag{33}$$

$$M = \Re e\{(\widehat{m}_x(y) i_x + \widehat{m}_y(y) i_y) e^{j\Omega t}\} + M_0 i_z \tag{34}$$

$$B = \mu_0 (H + M) \tag{35}$$

The relationship between M_0 and H_0, the z-directed components of magnetization and magnetic field intensity respectively, has been established in (21). There is no z-directed, small-signal magnetic field which, in turn means that there is no associated small-signal magnetization component along i_z. Therefore, the z-component of magnetization is DC and given by the equilibrium value of M_0. To solve for the instantaneous magnetization, the imposed fields, $\widehat{b}_y$ and $\widehat{h}_x$, are assumed known small-signal sources. Substituting for M_{eq} from (18) through (21) and for M from (34), the x and y (transverse) components of (22) are given by (36) and (37) respectively. Making use of (35), (36) and (37) are used to write solutions for $\widehat{m}_x$ and $\widehat{m}_y$ which are functions of spin-velocity, as given by (38) and (39).

$$j\Omega\widehat{m}_x + \omega_z\widehat{m}_y + \frac{1}{\tau}\left(\widehat{m}_x - \frac{M_0}{H_0}h_x\right) = 0 \tag{36}$$

$$j\Omega\widehat{m}_y - \omega_z\widehat{m}_x + \frac{1}{\tau}\left(\widehat{m}_y - \frac{M_0}{H_0}h_y\right) = 0 \tag{37}$$

$$\widehat{m}_x = \frac{M_0}{H_0} \frac{(j\Omega\tau + 1 + M_0/H_0)\widehat{h}_x - (\omega_z\tau)\widehat{b}_y/\mu_0}{(j\Omega\tau + 1)(j\Omega\tau + 1 + M_0/H_0) + (\omega_z\tau)^2} \tag{38}$$

$$\widehat{m}_y = \frac{M_0}{H_0} \frac{(\omega_z\tau)\widehat{h}_x + (j\Omega\tau + 1)\widehat{b}_y/\mu_0}{(j\Omega\tau + 1)(j\Omega\tau + 1 + M_0/H_0) + (\omega_z\tau)^2} \tag{39}$$

The complex amplitudes of transverse magnetization, $\widehat{m}_x$ and $\widehat{m}_y$, are a function of the yet undetermined spin-velocity ω_z. As will be shown in the subsequent analysis, in the absence of imposed flow, the spin-velocity (and hence $\widehat{m}_x$ and $\widehat{m}_y$) is spatially invariant. With the imposition of flow, the spin-velocity, as well as $\widehat{m}_x$ and $\widehat{m}_y$, then vary with channel width, y. The second term of (22) does not contribute any terms since the flow velocity is along i_x and $\frac{\partial}{\partial x}$ of the magnetization is zero. The magnetization in the ferrofluid gives rise to a torque which, in turn, is responsible for fluid motion causing a non-zero value for spin-velocity ω_z which changes the magnetization. Therefore, as well as the ferrofluid relaxation, one should consider the mechanical equations of interest to arrive at a consistent solution for $\widehat{m}_x$, $\widehat{m}_y$ and ω_z.

2.2.3 Fluid Mechanics—Applying the principles of conservation of linear and angular momentum to an incompressible ferrofluid leads to the simplified expressions of (40) and (42) respectively [1], [2] where p' is the modified pressure along the channel, given by (41), p is the absolute pressure in Pa, g is the gravitational acceleration acting along i_y in m·s^{-2}, ρ is the ferrofluid mass density in kg·m^{-3}, ζ is the ferrofluid vortex viscosity in N·s·m^{-2} which is approximately given by $\frac{3\eta\varphi}{2}$ for $\varphi \ll 1$ [2], η is the dynamic shear viscosity of the ferrofluid in N·s·m^{-2} and T_m is the magnetic torque density given by (43) in N·m^{-2}. The small-signal expressions consider the situation of sinusoidal steady state with viscous dominated flow conditions (so that inertia is negligible) and the ferrofluid only responds to force and torque densities which have a time-averaged, non-zero component. Also ignored are the coefficients of shear and bulk viscosity (η' and λ') [2] discussed by Elborai [27] and He [28] in reference to (42).

$$-\nabla p' + \mu_0(M \cdot \nabla)H + 2\zeta\nabla \times \omega + (\zeta+\eta)\nabla^2 v = 0 \tag{40}$$

$$p' = p + \rho g y \tag{41}$$

$$T_m + 2\zeta(\nabla \times v - 2\omega) = 0 \tag{42}$$

$$T_m = \mu_0(M \times H) \tag{43}$$

The conservation of linear momentum (neglecting inertial terms), shown in (40), contains terms due to (i) pressure and gravity, (ii) magnetic force density (given by the Kelvin force density), (iii) coupling to spin-velocity and (iv) viscosity. The spin-velocity, as indicated by the conservation of angular momentum (42), can be caused by two factors; (i) vorticity in the flow (due to the $\nabla \times v$ term) and (ii) due to a magnetic torque, T_m, arising when the magnetic field and the associated magnetization in the suspension, are no longer parallel. In the absence of a magnetic torque density (e.g., in a non-magnetic fluid), (42) reduces to the rotational momentum equation, neglecting inertial terms, where spin-velocity is due only to vorticity in the flow. For a magnetic fluid, in the absence of flow, the spin-velocity is proportional to the magnetic torque density and, thereby a measure of misalignment between the magnetic field and fluid magnetization. After time averaging, denoted by $\langle \rangle$, the only remaining non-zero component of magnetic torque density for the system, now expressed in terms of the applied fields from (43), is given by (44) where * denotes the complex conjugate.

$$\langle T_{m,z} \rangle = \frac{\mu_0}{2}\Re e(\widehat{m}_x\widehat{h}_y^* - \widehat{h}_x\widehat{m}_y^*) \tag{44}$$

Considering (35), one can rewrite the time-averaged torque density in terms of the imposed fields and the complex transverse magnetization amplitudes.

$$\langle T_{m,z}\rangle = \frac{1}{2}\Re e(\widehat{m}_x\widehat{b}_y^* - \mu_0(\widehat{h}_x+\widehat{m}_x)\widehat{m}_y^*)$$

(45)

Using (42), one can relate vorticity, spin-velocity and torque density as given by (46).

$$-2\zeta\frac{\partial v_x}{\partial y} - 4\zeta\omega_z + \langle T_{m,z}\rangle = 0$$

(46)

Considering (40), one should note that the second non-zero term, $\mu_0(\boldsymbol{M}\cdot\nabla)\boldsymbol{H}$, is the magnetic force density $\boldsymbol{F}_m$ associated with the ferrofluid. However for the geometric arrangement of Fig. 1, the field components can only vary with y so the only non-zero component of magnetic force density is y-directed and considering (31) and (35) given by (47). Again, only the non-zero, time-averaged terms are retained. The $\wedge$ symbol indicates the complex, small-signal amplitude.

$$F_{m,y} = \mu_0(m_x\frac{\partial h_y}{\partial x} + m_y\frac{\partial h_y}{\partial y} + (M_0)\frac{\partial h_y}{\partial z})$$
$$\Rightarrow F_{m,y} = \mu_0(m_y\frac{\partial h_y}{\partial y}) = -\mu_0(m_y\frac{\partial m_y}{\partial y})$$
$$F_{m,y} = -\frac{\mu_0}{2}\frac{\partial(m_y^2)}{\partial y}$$
$$\langle F_{m,y}\rangle = -\frac{\mu_0}{4}\frac{\partial|\widehat{m}_y|^2}{\partial y}$$

(47)

In light of the simplification of (47), one might write the non-zero components for (40) as given by (48) and (49). Conservation of linear momentum yields components along both $\boldsymbol{i}_x$ and $\boldsymbol{i}_y$, given by (48) and (49) respectively. There is no component along $\boldsymbol{i}_z$. Assuming that pressure may vary as a function of channel width and length (*i.e.*, $p = p(x, y)$), then integration of (49) leads to (50) where $f(x)$ is due to the x-directed flow velocity while the pressure's y-dependence is due (a) to gravity, as noted in (41) and (b) the y-dependence in m_y.

$$-\frac{\partial p'}{\partial x} + 2\zeta\frac{\partial \omega_z}{\partial y} + (\zeta+\eta)\frac{\partial^2 v_x}{\partial y^2} = 0$$

(48)

$$-\frac{\partial(p+\rho gy)}{\partial y} - \frac{\mu_0}{4}\frac{\partial|\widehat{m}_y(y)|^2}{\partial y} = 0$$

(49)

$$\Rightarrow p(x,y) + \rho gy + \frac{\mu_0}{4}|\widehat{m}_y(y)|^2 = f(x)$$

(50)

Equations (38), (39), (46) and (48) now constitute a closed system of equations with 4 unknown quantities: spin-velocity, ω_z, flow velocity, v_x, and the two complex amplitudes of magnetization along $\boldsymbol{i}_x$ and $\boldsymbol{i}_y$, denoted $\widehat{m}_x$ and $\widehat{m}_y$, respectively. It is again noted that $\widehat{b}_y$ and $\widehat{h}_x$ are imposed uniform small-signal fields and therefore known. While (50) is an additional equation of interest which accounts for changes in fluid pressure, it does not govern fluid flow. However, (50) does provide a way to measure $|\widehat{m}_y|$ from pressure measurements.

2.3 General Solutions

2.3.1 Boundary Conditions—Generalized analytical solutions of (38), (39), (46) and (48) can be obtained subject to boundary conditions. From Maxwell's Equations, the relevant boundary conditions on the magnetic field components are given by (51) and (52) where i_n is the unit vector normal to the boundary in the second medium. K_s is the boundary surface current density in A·m^{-1} at $y = 0$ and $y = d$ for Figure 1 which is the source for the x-directed and z-directed magnetic fields. The magnetic flux density and magnetic field intensity, given by B_{in} and H_{in} respectively, correspond to the fields on the inside of the ferrofluid region (*i.e.*, $0 < y < d$) while B_{out} and H_{out} correspond to the fields outside the ferrofluid (*i.e.*, $y < 0$ and $y > d$). The surface currents at $y = 0$ and $y = d$ must be opposite in direction (x-directed DC surface current to generate a uniform DC z-directed field and z-directed time-varying surface current to generate a time-varying x-directed field) so that the magnetic fields outside the ferrofluid region are zero. For the y-directed B field, the field is imposed upon the channel when magnetic pole faces are located at $y = 0$ and $y = d$.

$$i_n \cdot (B_{in} - B_{out}) = 0 \tag{51}$$

$$i_n \times (H_{in} - H_{out}) = K_s \tag{52}$$

There are no boundary conditions on the spin velocity, ω_z, as the spin viscosity is not considered in (42), while the velocity, v_x, at the stationary boundaries ($y = 0$ and $y = d$) is also zero.

2.3.2 Poiseuille Flow Solution—Poiseuille flow is achieved in the channel by means of an x-directed pressure differential which, in the absence of a magnetic torque density in the fluid, results in a parabolic flow profile with y which is approximated by blood flow in the medium to large human vessels. The x-component of (40) has pressure gradient, spin velocity, and viscous flow contributions.

Differentiating (46) and writing in terms of $\frac{\partial \omega_z}{\partial y}$ allows for simplification of (48) by substitution of the $\frac{\partial \omega_z}{\partial y}$ term from (53).

$$\frac{\partial \omega_z}{\partial y} = \frac{1}{4\zeta} \frac{\partial \langle T_{m,z} \rangle}{\partial y} - \frac{1}{2} \frac{\partial^2 v_x}{\partial y^2} \tag{53}$$

This leads to the expression of (57) after twice integrating (48) with respect to y. K_1 and K_2 are constants of integration while $\langle T_{m,z} \rangle$ is given by (45).

$$-\frac{\partial p'}{\partial x} + 2\zeta \left(\frac{1}{4\zeta} \frac{\partial \langle T_{m,z} \rangle}{\partial y} - \frac{1}{2} \frac{\partial^2 v_x}{\partial y^2} \right) + (\zeta + \eta) \frac{\partial^2 v_x}{\partial y^2} = 0 \tag{54}$$

$$\Rightarrow -\frac{\partial p'}{\partial x} + \frac{1}{2} \frac{\partial \langle T_{m,z} \rangle}{\partial y} + \eta \frac{\partial^2 v_x}{\partial y^2} = 0 \tag{55}$$

$$\Rightarrow -\frac{\partial p'}{\partial x}y+\frac{1}{2}\langle T_{m,z}\rangle+\eta\frac{\partial v_x}{\partial y}+K_1=0 \tag{56}$$

$$\Rightarrow -\frac{\partial p'}{\partial x}\frac{y^2}{2}+\frac{1}{2}\int_0^y\langle T_{m,z}\rangle dy'+\eta v_x+K_1 y+K_2=0 \tag{57}$$

Applying the non-slip boundary conditions on v_x at $y = 0$ and d allows for the solution of K_1 and K_2.

$$v_x(0)=0 \Rightarrow K_2=0 \tag{58}$$

$$v_x(d)=0 \Rightarrow K_1=\frac{d}{2}\frac{\partial p'}{\partial x} - \frac{1}{2d}\int_0^d\langle T_{m,z}\rangle dy' \tag{59}$$

Substituting the results of (58) and (59) into (57) and rearranging one arrives at (60).

$$\Rightarrow v_x=\frac{1}{2\eta}\frac{\partial p'}{\partial x}(y^2 - yd) - \frac{1}{2\eta}\left(\int_0^y\langle T_{m,z}\rangle dy' - \frac{y}{d}\int_0^d\langle T_{m,z}\rangle dy'\right) \tag{60}$$

Rewriting (46) as (61) and substituting for the derivative of v_x leads to the following expression for the spin-velocity, ω_z, which is independent of v_x and where $\langle T_{m,z}\rangle$ is given by (45).

$$\frac{\partial v_x}{\partial y}=\frac{1}{2\zeta}\langle T_{m,z}\rangle - 2\omega_z \tag{61}$$

$$\omega_z= -\frac{1}{4\eta}\frac{\partial p'}{\partial x}(2y - d)+\langle T_{m,z}\rangle\frac{\eta+\zeta}{4\zeta\eta} - \frac{1}{4d\eta}\int_0^d\langle T_{m,z}\rangle dy' \tag{62}$$

While (62) is not solvable analytically, it can be solved numerically and the results which follow use *Comsol Multiphysics* (COMSOL AB, Stockholm, Sweden) to do that.

The simplest case is when $\langle T_{m,z}\rangle$ is negligibly small, in which case, spin-velocity is given by (63) and the mid-channel spin-velocity is zero (*i.e.,* $\omega_z(y=\frac{d}{2})=0$). This is the case of "vorticity-driven" spin-velocity.

$$U_p = -\frac{d^2}{8\eta}\frac{\partial p'}{\partial x}$$
$$\Rightarrow \omega_z(y=0) = -\omega_z(y=d) = \frac{d}{4\eta}\frac{\partial p'}{\partial x} = -\frac{2U_p}{d} \tag{63}$$

The resulting Poiseuille flow has flow velocity profile given by (64) with a maximum value, U_p, at $y = d/2$.

$$\Rightarrow v_x(y) = \frac{1}{2\eta}\frac{\partial p'}{\partial x}y(y-d) = \frac{4}{d^2}U_p y(y-d) \tag{64}$$

$$\Rightarrow v_x(d/2) = -\frac{d^2}{8\eta}\frac{\partial p'}{\partial x} = U_p \tag{65}$$

Another interesting limiting case is conditions of negligible flow in the channel (*i.e.*, $v_x(y) = 0$). Then ω_z, $\hat{m}_x$, $\hat{m}_y$ and $\langle T_{m,z}\rangle$ are independent of y so that ω_z reduces to (67).

$$\omega_z = \langle T_{m,z}\rangle\frac{\eta+\zeta}{4\zeta\eta} - \frac{1}{4d\eta}\int_0^d\langle T_{m,z}\rangle dy = \frac{1}{4\zeta}\langle T_{m,z}\rangle \tag{66}$$

$$\omega_z = \frac{1}{8\zeta}\Re e(\widehat{m}_x\widehat{b}_y^* - \mu_0(\widehat{h}_x + \widehat{m}_x)\widehat{m}_y^*) \tag{67}$$

Substituting for $\hat{m}_x$ and $\hat{m}_y$ from (38) and (39) respectively yields a cubic solution for the spin-velocity, ω_z. The no-flow solution ($v_x = 0$) is examined in the Results of Section 3 since it represents the contribution to spin-velocity and transverse fluid magnetization due only to the applied transverse magnetic field in the absence of any imposed fluid flow, a situation typical in low-perfusion MR imaging (e.g., breast tissue imaging).

3 Results

3.1 Physical Parameters

The physical parameters for the simulated magnetic nanoparticles are shown in Table 1 as well as the nominal field conditions. $U_p = v_x(y = d/2)$, from (65), denotes the maximum imposed inflow velocity under conditions of Poiseuille flow.

The main DC B_0 field is directed along $\boldsymbol{i}_z$. An approximately rotating field of constant amplitude is generated in the transverse xy plane by setting $\hat{h}_x = H_e$ and $\hat{b}_y = jB_e$ where B_e and H_e are real-valued quantities. A purely rotating field is difficult to achieve since the transverse magnetization components, $\hat{m}_x$ and $\hat{m}_y$, will clearly influence the fields within the fluid. However, when $H_e \gg \hat{m}_x, \hat{m}_y$ and B_e is set to be $\mu_0 H_e$, one can assume an approximate rotating magnetic field. The resultant transverse field rotates in a clockwise sense about the z axis for $H_e, B_e > 0$. The magnetic particle properties are typical of those used as superparamagnetic contrast agents in MRI [8,10,30] and similar to those proposed in magnetic nanoparticle

hyperthermia [11] and targeted drug delivery within MRI [12]. The magnetic core is assumed to be magnetite (Fe_3O_4). The radian frequency of excitation, denoted Ω, of the transverse rotating field varies but is normalized with respect to the ferrofluid time constant τ in the resulting plots. The non-dimensional spin-velocity is defined as $\omega_z\tau$. The ferrofluid dynamic viscosity, η, is that recorded by He [28] using 3% solid volume *MSG-W11* water-based ferrofluid from the *Ferrotec Corporation*, Bedford, New Hampshire. The nominal concentration of 0.03 solid volume fraction is approximately three orders of magnitude greater than the recommended *in vivo* concentration of Feridex, the most widely used commercial SPIO MRI contrast agent, used for liver imaging [29] although such high concentrations may well prove necessary in applications such as nanoparticle hyperthermia. The reasons for this adjustment are outlined in the discussion of Section 4.

The effect of varying the physical system parameters is examined for the normalized spin-velocity, $|\omega_z|\tau$, and the magnitude of the time-average transverse magnetization, $\langle|M_{trans}(y)|\rangle$. Referring to (34), one might write $\langle|M_{trans}(y)|\rangle$ as given by (71). For non-dimensionalized plotting, the transverse magnetization is normalized with respect to B_e by dividing by B_e/μ_0.

$$M_{trans}(y,t)=\Re\{(\widehat{m}_x(y)\boldsymbol{i}_x+\widehat{m}_y(y)\boldsymbol{i}_y)e^{j\Omega t}\} \tag{68}$$

$$|M_{trans}(y,t)|=\sqrt{(\Re e\{\widehat{m}_x(y)e^{j\Omega t}\})^2+(\Re e\{\widehat{m}_y(y)e^{j\Omega t}\})^2} \tag{69}$$

$$\langle|M_{trans}(y,t)|\rangle=\frac{1}{\sqrt{2}}\sqrt{\left|\widehat{m}_x(y)\right|^2+\left|\widehat{m}_y(y)\right|^2} \tag{70}$$

$$\langle|M_{trans}(y,t)|\rangle=\frac{1}{\sqrt{2}}\sqrt{(\Re e\{\widehat{m}_x(y)\})^2+(\Im m\{\widehat{m}_x(y)\})^2+(\Re e\{\widehat{m}_y(y)\})^2+(\Im m\{\widehat{m}_y(y)\})^2} \tag{71}$$

The results which follow examine the magnitude of the time-average transverse magnetization. The transverse magnetization will, in general, be elliptically polarized in the *xy* plane since $\widehat{m}_x$ and $\widehat{m}_y$ can differ in both magnitude and phase.

3.2 Results with No Imposed Flow

The case of no imposed flow was examined for a 5 mm wide channel. This represents an approximate resolution limit for low-field MRI [23]. The effect of changing the MRI's DC B_0 field on both the normalized spin velocity, $\omega_z\tau$, and the time-average transverse magnetization, normalized with respect to B_e were investigated. The results are shown in Fig. 3(a) and (b). Also investigated was the magnetization's dependence on ferrofluid concentration, φ, shown in Fig. 4(a) versus normalized time, Ωt (shown for $\Omega\tau = 1$ over one full cycle), and in Fig. 4(b) versus normalized frequency, $\Omega\tau$. The plots were achieved using *Mathematica 5.2* (Wolfram Research, Champaign, IL) with reference to (38), (39) and (67) where *Mathematica* was used to express and plot the solutions in closed form. In each case, the *x*-axis is the non-dimensional transverse rotating field frequency $\Omega\tau$, the rotating field amplitude, B_e, is 5% of B_0 and $\varphi = 3\%$.

3.3 Imposing Poiseuille Flow

Poiseuille flow conditions were implemented by means of an imposed flow profile on the left-most entry to the channel of Fig. 1 rather than an imposed pressure differential across the channel. This approach allowed the maximum flow velocity in the channel to be defined as U_p for Poiseuille flow conditions. Finite element simulation and solution of the variables in the channel is achieved using *Comsol Multiphysics* where (38) through (44) are the equations of interest, in the case of Poiseuille flow. Boundary conditions of zero flow are imposed upon the upper and lower plates as is the case for no imposed flow. However, inlet flow (defined from the left side) is *x*-directed and defined by the parabolic distribution of (72) where *d* is the channel width while the outlet boundary condition defines the pressure, $p = 0$. The channel length was set to 100*d* in the numerical channel simulations using *Comsol Multiphysics*.

$$v_{in,x}(y) = \frac{4U_p y(d - y)}{d^2}$$

(72)

The result of the imposed parabolic flow profile in the channel is that the spin-velocity is no longer spatially invariant as in the previous case. The total spin-velocity in the channel is now the sum of contributions from the Poiseuille imposed flow condition and the time-averaged magnetic torque density, $\langle T_{m,z} \rangle$. Since the flow-induced spin-velocity changes sign at $y = d/2$, the two contributions to the spin-velocity (from (i) the imposed fields and (ii) the imposed flow) will sum positively for $d/2 < y < d$ and sum negatively for $0 < y < d/2$. For the geometry of Fig. 1 where flow is directed along $+\mathbf{i}_x$, the contributions to ω_z from the imposed rotating field, B_e, and that due to Poiseuille flow, add at the lower plate and subtract at the top so that the maximum value of $|\omega_z|\tau$ occurs at $y = 0$ and $y = d$. In the results of Fig. 5, the channel width (1 μm) and imposed maximum flow velocity ($0.1 < U_p < 1$ m/s) are chosen so that the spin-velocity, and hence changes in the transverse magnetization as a function of channel width, *y*, are almost entirely due to the imposed flow rather than the applied rotating field. Fig. 5 shows the normalized spin-velocity and normalized, time-average transverse magnetization across the channel width for various maximum imposed flow velocities: $U_p = 0.1$ m/s, 0.5 m/s and 1 m/s and when $\Omega\tau = 1$ to maximize the effect of spin-velocity and $B_0 = 0.2$ T. These flow velocities represent the maximum range of blood flow velocities *in vivo* where the magnetic nanoparticle suspension might potentially flow.

4 Discussion

The unusual behavior of magnetic fluid in the presence of rotating magnetic fields is well understood [1,2]. This work now adds the strong DC field associated with MRI and examines the simulated behavior of these fluids in a planar channel. The effect of nanoparticle rotation in the presence of a transverse rotating field (amplitudes between 1% to 10% of B_0) was considered. While this represents a significant modification of the low-field MRI system, one should bear in mind the recent additions and modifications proposed to MRI magnetic fields for a variety of biomedical applications including hyperthermia and targeted drug delivery [11,12]. These include the addition of an RF hyperthermia coil to 1.5 T MRI [32] which operated a time-sharing arrangement between image acquisition and therapy.

As the transverse rotating magnetic field frequency increases such that $\Omega\tau \to 1$, the fluid's transverse magnetization component and the applied rotating field become increasingly misaligned due to the magnetic torque density on the fluid and the transverse magnetization's magnitude is a strong function of $\Omega\tau$. The ferrofluid spin-velocity, ω_z, was introduced as a measure of nanoparticle spin or rotation [1]. In the absence of fluid flow ($\mathbf{v} = \mathbf{0}$) in a magnetic fluid, the spin-velocity is proportional to the magnetic torque density of the fluid suspension,

as given in (42) (or in physical terms, the spin-velocity is proportional to the instantaneous misaligment which occurs between the fluid's magnetization and the applied magnetic field). However, with the introduction of linear flow, the particle rotation (and hence the spin-velocity in the fluid) will be altered due to any vorticity that may be present in the flow as well as due to the magnetic torque density, as governed by (42).

4.1 Spin-velocity dependence on rotating field frequency Ω

Spin-velocity was introduced as a measure of magnetic nanoparticle rotation within the fluid suspension due to the rotating transverse magnetic field in the MRI. The dependence of the fluid spin-velocity, ω_z, is closely related to the ferrofluid time constant, τ, as should be expected from the expressions of (38) and (39) since $\omega_z \tau$ is a term that appears in both the numerator and denominator of each expression. For low-frequencies where $\Omega\tau \ll 1$ and $\omega_z\tau \ll 1$, the effect of spin-velocity on the fluid's transverse magnetization is negligible. Physically this low-frequency limit corresponds to a fluid with a small-signal transverse susceptibility given by M_0/H_0 and the instantaneous transverse $\boldsymbol{M}$ and $\boldsymbol{H}$ vectors are almost collinear.

As $\Omega\tau$ approaches unity, the spin-velocity becomes increasingly significant. This is because the time constant of the suspension, τ, is no longer fast enough to allow the particles to reestablish transverse equilibrium before the excitation changes direction, due to the rotating transverse field. Instead, synchronism is maintained at a constant lag angle between the transverse components of $\boldsymbol{M}$ and $\boldsymbol{H}$ for a particular rotating field frequency Ω. Mathematically, this is shown by the on-axis magnetization (both $\hat{m}_x$ and $\hat{m}_y$) given by (38) and (39) becoming increasingly dependent on the orthogonal transverse field component, $\hat{h}_x$, for the case of $\hat{m}_y$, and $\hat{b}_y$ for the case of $\hat{m}_x$. (*i.e.*, the effect of $\hat{b}_y$ in (38) and the effect of $\hat{h}_x$ in (39) increases). This cross-coupling results in a non-symmetric, small-signal transverse susceptibility which causes $\boldsymbol{M}_{trans}$ to lag transverse magnetic field excitation as previously noted.

In the high-frequency limit, where $\Omega\tau \gg 1$, the denominators of (38) and (39) become the dominant terms. The spin-velocity is less significant in the transverse magnetization and in the limit of $\Omega\tau \gg 1$, the transverse magnetization becomes negligible so that the ferrofluid no longer appears magnetic in the transverse *xy* plane. It is noted that this scenario is very difficult to achieve in reality since the typical time constant of 1 μs requires $\Omega/(2\pi)$ on the order of 1.6 MHz before $\Omega\tau \approx 10$. However, it can be intuitively expected that finite fluid viscosity limits nanoparticle rotation at high frequency. Shliomis [1] notes that his formulation is no longer valid in the frequency range of $\Omega\tau \gg 1$ so that the plots should be treated with some caution beyond $\Omega\tau \approx 10$. The *z*-directed magnetization, M_0, is DC as previously noted ($h_z = 0$) and is given by (21) throughout. The point of this portion of the analysis is that the interaction between the rotating magnetic field and nanoparticle's transverse magnetization is optimized at $\Omega\tau = 1$ within the MRI, as indicated by the peak in spin-velocity, as shown in Figure 3(a).

4.2 No Imposed Flow

In the absence of externally imposed flow, the ferrofluid spin-velocity is spatially constant in the channel of Fig. 1. As noted, the maximum spin-velocity occurs when $\Omega\tau = 1$ and increases with the main *z*-directed B_0 field, as shown in Fig. 3(a). However, the time-average transverse magnetization seen in Figure 3(b) decreases with B_0. This is because when B_0 is increased, the small-signal susceptibility for the transverse components, M_0/H_0 shown in Figure 1, decreases. So while the value of spin-velocity increases, the underlying coupling between the small-signal transverse field perturbation (h_x or h_y) and the associated instantaneous magnetization components (with complex amplitudes given by (38) and (39)), is weakened with larger B_0. Physically, this effect with increasing B_0 can be interpreted as the increasing probability (as determined by the Langevin relation) of each individual magnetic nanoparticle remaining parallel to B_0 rather than rotating in the transverse plane in response to the transverse B_e field.

The result is a decrease in the fluid's transverse magnetization component with increasing B_0.

The time-dependence of the transverse magnetization is shown in Figure 4(a) for various values of $\Omega\tau$ and $\varphi = 0.05$. Clearly, as predicted by (71), the phase lag behind the sinusoidal B_e field is more pronounced as $\Omega\tau$ increases where the instantaneous transverse magnetization has an inflection point that lags that of the sinusoidal B_e field. It is this phase-lag between the transverse M and H fields which gives rise to a non-zero magnetic torque density in the magnetic fluid. The effect of φ, shown in Figure 4(b) on the time-average transverse magnetization is pronounced and arises from the dependence of the saturation magnetization, $M_s = \varphi M_d$, causing the normalized time-average transverse magnetization $\langle|M_{trans}|\rangle$ increases with φ.

In no case does the value of normalized transverse magnetization become comparable to B_e/μ_0. Even for the conditions of Figure 3(b) where $B_0 = 0.1$ T and $B_e = 5\%$ of B_0, the normalized magnetization is only 11% of H_e for the low-frequency limit discussed previously. This indicates that it may be difficult to observe the frequency-dependence of the transverse magnetization in low-field MRI since the change in the transverse magnetization is in addition to (i) the main B_0 and (ii) the applied rotating field used to generate it. However, non-MRI imaging modalities, such as magnetic particle imaging (MPI) [14] may be suitable. In MPI, it is the magnetization associated with the magnetic nanoparticles themselves which give rise to signal rather than the imaging spin of the hydrogen proton, as is the case in MRI.

The transverse magnetization decreases as $\Omega\tau$ approaches unity since the increasing misalignment of the M and H fields is accompanied by a decrease in the absolute magnitude of the transverse magnetization. This decrease results from the dominance of the denominator in (38) and (39) as $\Omega\tau$ increases. The point here is that the applied transverse magnetic field controls the transverse magnetization of the fluid, where the frequency, Ω, effectively acts as the amplitude dial on the transverse magnetization. This presents the possibility of an interactive fluid magnetization mechanism, controlled by the applied magnetic field frequency and amplitude. It would be evident that the role of the transverse magnetization is in addition to that of the DC magnetization due to B_0 (which is not controllable in an interactive sense). However, imaging modalities do exist where the B_0 field is pulsed (*e.g.*, prepolarized MRI (pMRI) [31] where pulsed electromagnets produce diagnostic quality 0.5 to 1.0 T images with significantly reduced cost and susceptibility artifacts) or eliminated entirely (*e.g.*, magnetic particle imaging (MPI) [14] uses strong magnetic field gradients to generate a moving point of zero-field where the magnetic nanoparticles are unsaturated for direct imaging of their distribution in the absence of a B_0 field). In MPI, the signal is not the imaging protons of the hydrogen proton (as in MRI) but rather the magnetization of the magnetic particles, as investigated in this work. The addition of an oscillating field (10 mT drive field arbitrarily chosen at a frequency of 25 kHz) to the gradient fields move the zero-field point over the field of view, inducing a signal where the nanoparticles are present. Since the oscillating field frequency was determined without regard to τ, it may be possible to reconfigure the system to allow $\Omega\tau$ approach unity and examine the modified effects on the fluid magnetization. A proposed investigative system might consist of the commercial MRI contrast agent, *Feridex* (Advanced Magnetics, Cambridge, MA), a rotating field amplitude of 10 mT and a frequency range of 50–300 kHz, such that operation in the $\Omega\tau \sim 1$ range might be achieved. Under such conditions, one should expect significant changes in the fluid magnetization (the signal source in MPI) as a function of rotating field frequency and amplitude where $\Omega\tau$ approaches unity.

4.3 Imposing Poiseuille Flow

Imposing conditions of Poiseuille flow on the channel of Fig. 1 shows significant change from the preceding case of no imposed flow since, now, the spin-velocity and transverse

magnetization are functions of the channel width along y. As already noted, the channel width and flow velocities are chosen such that the flow vorticity, and not the magnetic torque density, is the dominant source for the spin-velocity and subsequent changes in transverse magnetization. Comparing (63) with (64) yields the limit of the maximum spin-velocity in a vorticity-driven planar flow system, given by (73). Inspection of Figure 5 shows that this is the case for the three values of U_p evaluated (*i.e.*, the maximum normalized spin velocity, $\omega_z\tau$, has values of 0.2, 1 and 2 when $U_p = 0.1$, 0.5 and 1 m/s respectively where $d = 1\mu$m and $\tau = 1\mu$s).

$$|\omega_{z,max}|\tau \to \frac{2U_p}{d}\tau \tag{73}$$

The transverse magnetization's dependence on the spin-velocity now gives rise to a non-uniform magnetization across the channel width for vorticity-dominated spin-velocity, as shown in Figure 5(b). Although channel widths on the order of μm simulated here are not currently resolved in low-field MRI due to decreased SNR, this non-uniformity in the magnetization is a function of the flow velocity. The effect does not persist as B_0 is increased (e.g., 1.5 T or 3 T) due to magnetic saturation. The dependence on spin-velocity (and hence on U_p for a vorticity-driven system) is involved as seen from (38) and (39) in conjunction with (62). For small U_p, typical of physiological flow (~0.1 m/s), the normalized spin velocity term ($\omega_z\tau$) in the numerator dominates and the magnetization is approximately a linear function of the channel width, y. With increasing U_p ~1 m/s, it is found the $\omega_z^2\tau^2$ term of the denominator becomes significant, resulting in the non-linear functions of y shown in Fig. 5(b). The point here is that what was previously a uniform fluid magnetization in the transverse plane is now non-uniform due to the nanoparticle flow in narrow channels. The effect provides a second mechanism of interaction with the fluid's magnetization. While effects due to flow vorticity many not be readily applicable in the physiological environment (due to (i) the high particle concentrations of nanoparticles required to see effects in the vasculature and (ii) the combination of high-flow velocities and narrow channels necessary to create the necessary vorticity), the effect is noted and may be more relevant to non-clinical scenarios such as pipe-flow monitoring with magnetic or magnetically-doped flow.

5 Conclusion

This work examines the dynamic behavior of magnetic nanoparticle suspensions in the low-field MRI environment with the addition of a strong rotating magnetic field transverse to the MRI's main DC field. It is shown that under circumstances of high local nanoparticle concentrations (~0.05 solid volume fraction) and low field MRI (~0.1 to 0.35 T), the fluid's transverse magnetization shows strong dependence on the rotating field frequency, as shown in Figures 3(b) and 4. At high MRI field strengths (1.5 T and 3 T) assuming the rotating field amplitude remains in the mT range considered in this work, the effects decrease significantly (as evident from Figure 3(b)) due to the ferrofluid's magnetic saturation. However, at low field MRI where rotating field amplitudes in the mT range are more easily realized, the transverse ferrofluid magnetization magnitude can be significantly decreased by decreasing field frequency. It is proposed that the phenomenon might be investigated by means of the recently proposed imaging modality of magnetic particle imaging [14], where the system frequency is modified to allow $\Omega\tau$ approach unity, thus enabling nanoparticle rotation dynamics to alter the fluid magnetization, and potentially, image contrast in MPI where fluid magnetization is the signal source.

It was further shown that the fluid's transverse magnetization can be significantly altered by the presence of the ferrofluid in the channel of Fig. 1 as a function of increasing flow velocity since vorticity in the flow induces spin-velocity. Application of this phenomenon may prove difficult in the physiological environment due to the significant vorticity, not typical of clinical flow, and the high concentrations of magnetic nanoparticles required to see the effect.

The effects outlined in this work have not been previously examined in the MRI environment and so, this work should be of interest, not only to those using magnetic nanoparticles as MRI contrast agents, but also those exploiting magnetic nanoparticles for other *in vivo* applications. These include targeted drug delivery and magnetic nanoparticle hyperthermia but, perhaps most significantly, for MPI, where the effects outlined here may give rise to interactive ferrofluid magnetization due to the dynamic behavior of the magnetic nanoparticles in response to rotation.

Acknowledgments

References

1. Shliomis M. Soviet Physics JETP 1972;34:1291.

2. Rosensweig, RE. Ferrohydrodynamics. Dover Publications; New York, New York: 1997.

3. Shliomis M. Phys Rev E 2001;64

4. Shliomis M. Phys Rev E 2001;64

5. Shliomis M, Raikher Y. IEEE Trans Magn 1980;16:237250.

6. Pshenichnikov AF. Fluid Dyn 1996;31

7. Popplewell J, Rosensweig R, Johnston RJ. Magnetic field induced rotations in ferrofluids. IEEE Trans Magn 1990;26:1852–1854.

8. Weissleder R, Elizondo G, Wittenberg J, Rabito CA, Bengele HH, Josephson L. Ultrasmall superparamagnetic iron oxide: characterization of a new class of contrast agents for MR imaging. Radiology 1990;175:489–493. [PubMed: 2326474]

9. Mandeville JB, Moore J, Chesler DA, Garrido L, Weissleder R, Weisskoff RM. Dynamic liver imaging with iron oxide agents: Effects of size and biodistribution on contrast. Magn Res Med 1997;37:885–890.

10. Wang YJ, Hussain SM, Krestin GP. Eur J Radiol 2001;11:2319–2231.

11. Hergt R, Dutz S, Muller R, Zeisberger M. J Phys-Condens Mat 2006;18:S2919–S2934.

12. Forbes ZG, Yellen BB, Halverson DS, Fridman G, Barbee KA, Friedman G. IEEE T Bio-Med Eng 2008;55:643–649.

13. Tamaz S, Gourdeau R, Chanu A, Mathieu J-B, Martel S. IEEE T Bio-Med Eng 2008;55:1854–1863.

14. Gleich B, Weizenecker J. Nature 2005;435:1214–1217. [PubMed: 15988521]

15. Yeary LW, Moon JW, Love LJ, Thompson JR, Rawn CJ, Phelps TJ. IEEE Trans Magn 2005;41:4384–4389.

16. Morais RP, Goncalves GRR, Skeff Neto K, Pelegrini F, Buske N. IEEE Trans Magn 2002;38:3225–3227.

17. Gillis P, Koenig SH. Magn Res Med 1987;5:232–245.

18. Muller R, Gillis P, Moiny F, Roch A. Magn Res Med 1991;22:178–182.

19. Koenig SH, Kellar KE. Magn Res Med 1995;34:227–233.

20. Gillis P, Roch A, Brooks RA. J Magn Res 1999;137:402–407.

21. Zahn M, Greer DR. J Magn Magn Mater 1995;149:165–173.

22. Batchelor, GK. An Introduction to Fluid Dynamics. Cambridge, England: Cambridge University Press; 2000.

23. Haacke, EM.; Brown, RW.; Thompson, MR.; Venkatesan, R. Magnetic Resonance Imaging: Physical Principles and Sequence Design. New York, NY: John Wiley and Sons; 1999.

24. Patz, S., et al. presented at the 14th Scientific Meeting and Exhibition of Int. Society of Magnetic Resonance in Medicine; Seattle, WA. May 6–12, 2006;

25. Cantillon-Murphy, P. PhD Thesis. Massachusetts Institute of Technology; 2008. On the dynamics of magnetic nanoparticles in MRI.

26. Zahn, M.; Adalsteinsson, E. Systems and Methods for Tuning Properties of Nanoparticles. United States Patent Application. 11/525,234.

27. Elborai, SM. PhD dissertation. Dept. Elect. Eng. and Comp. Sci., Massachusetts Institute of Technology; Cambridge, MA: 2006.

28. He, X. PhD dissertation. Dept. Elect. Eng. and Comp. Sci., Massachusetts Institute of Technology; Cambridge, MA: 2006.

29. Feridex Patient Information. AMAG Pharmaceutical; Cambridge, Massachusetts: www.berlex.com/html/products/pi/Feridex_PI.pdf

30. Bjornerud A, Johansson L. NMR Biomed 2004;17:465–477. [PubMed: 15526351]

31. Morgan P, Conolly S, Scott G, Macovski A. Magn Res Med 1996;38:527–536.

32. Delannoy, J.; LeBihan, D.; Levin, R.; Hoult, D. Hyperthermia system combined with MRI unit. Proceedings of the Annual International Conference of the IEEE Engineering in Medicine and Biology Society; 1998. p. 344-345.

33. Hergt R, Dutz S. Magnetic particle hyperthermia - biophysical limitations of a visionary tumour therapy. Journal of Magnetism and Magnetic Material 2007;31:187–192.
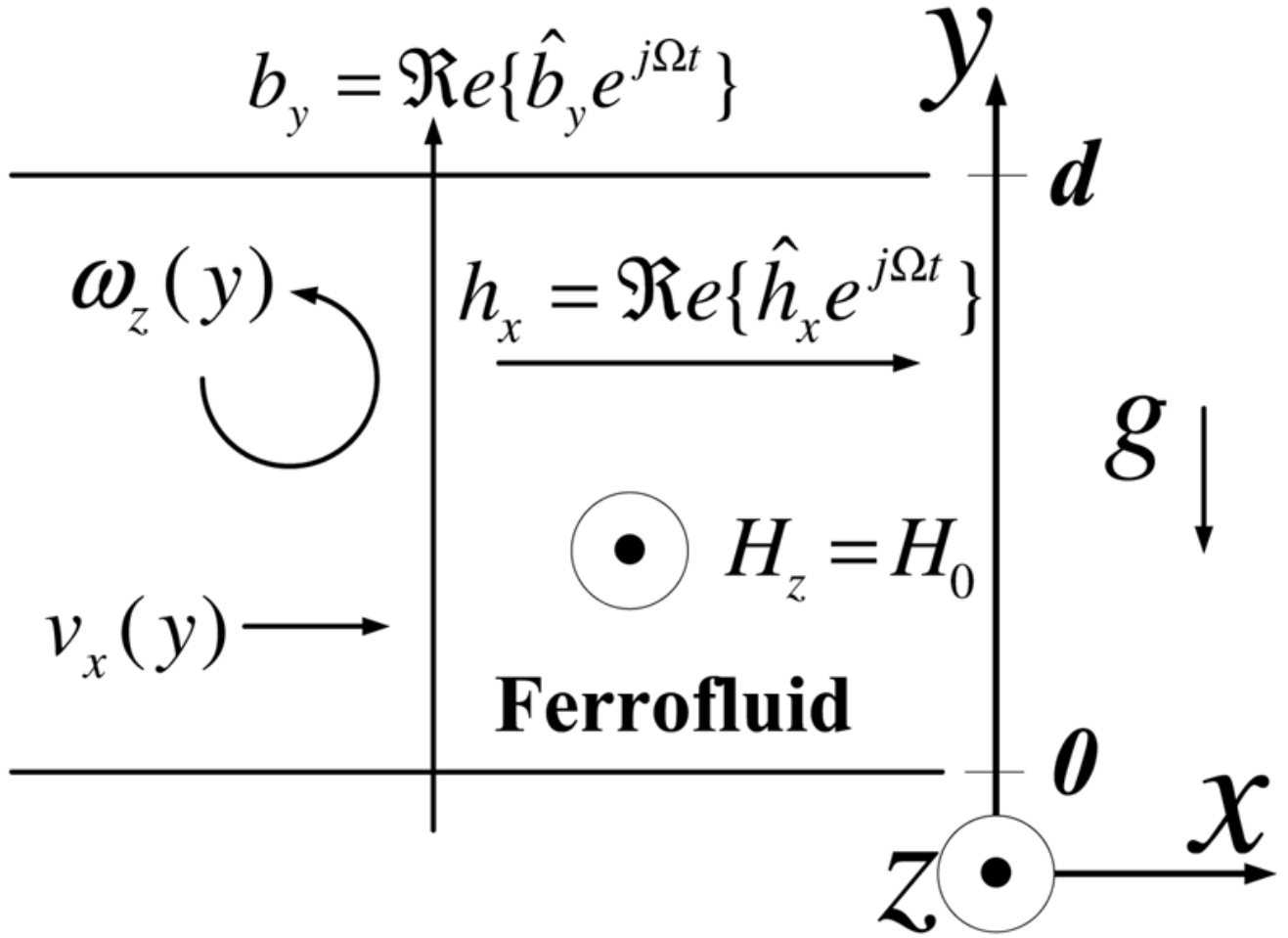
Fig. 1.
A planar ferrofluid layer between rigid and stationary walls (at $y = 0$ and $y = d$) is magnetically stressed by a uniform DC z-directed magnetic field H_0, an x-directed small-signal sinusoidal magnetic field with complex amplitude $\hat{h}_x$ and a y-directed small-signal sinusoidal magnetic flux density with complex amplitude $\hat{b}_y$. The x and y magnetic field components vary sinusoidally at frequency Ω. The velocity $v_x(y)$ is taken to be x-directed and the spin velocity, $\omega_z(y)$ is taken to be z-directed where both only depend on the y coordinate.

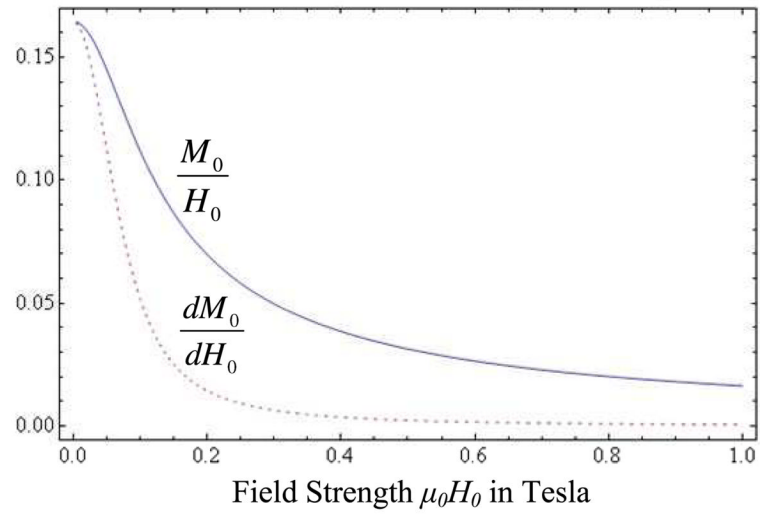**Effect of Main Field on the Small-Signal Susceptibility**

Fig. 2.

The values of the chord susceptibility, M_0/H_0, and the tangent susceptibility, $\frac{dM_0}{dH_0}$, are plotted for the parameters of Table 1 including a particle core radius of 4 nm. As expected, the values converge in the low-field limit where $\alpha_0 \ll 1$ and M_0 is proportional to H_0.
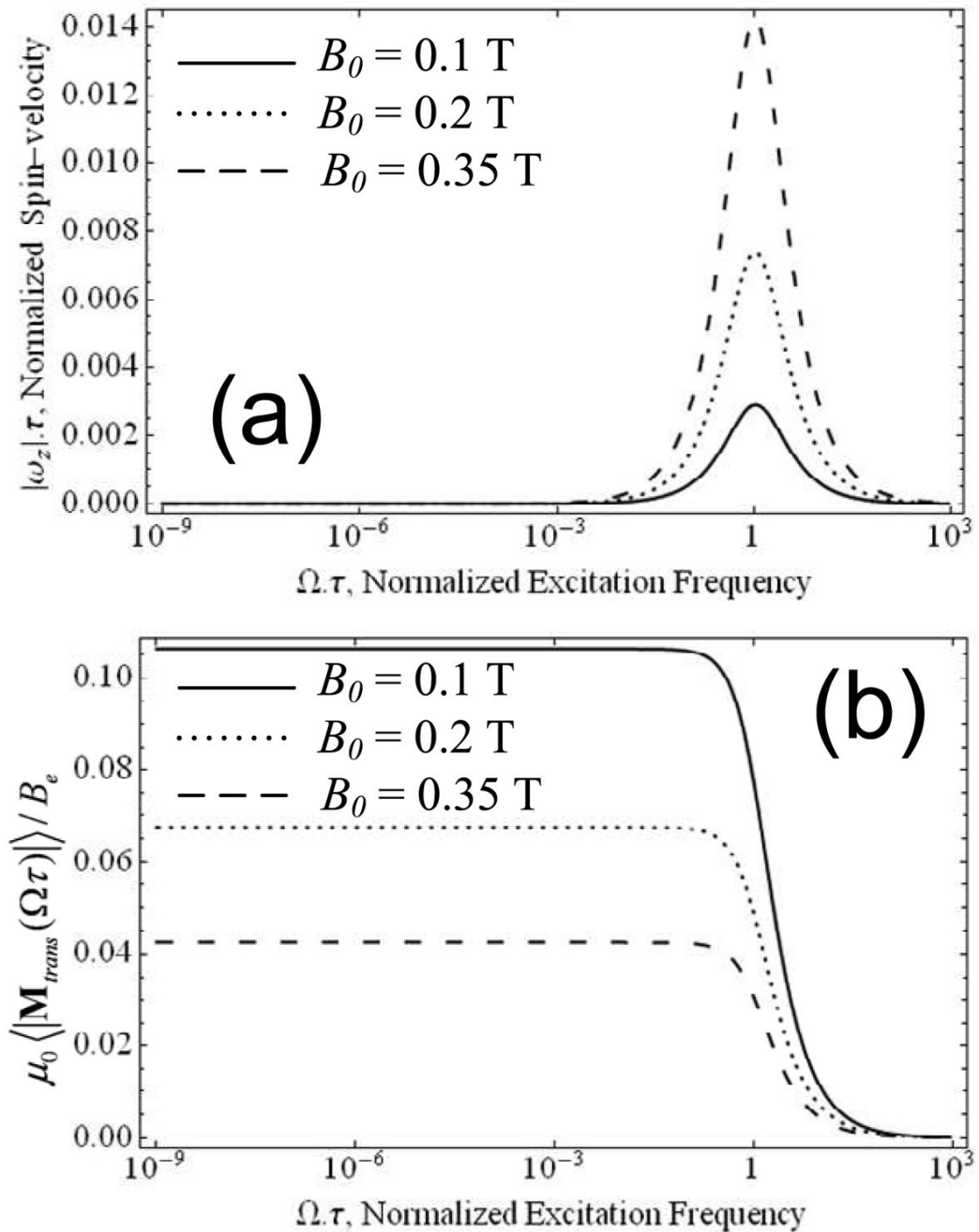
Fig. 3.
Frequency dependence of $|\omega_z|\tau$ and the normalized, time-average transverse magnetization on B_0 is shown for $\varphi = 3\%$ and $B_e = 0.05B_0$. Note that for $\tau = 1$ μs, $\Omega/(2\pi) \approx 160$kHz when $\Omega\tau = 1$. The channel width, $d = 5$ mm in each case and there is no imposed flow. For the case of clockwise rotating field with respect to the z axis, the direction of the spin-velocity is along $-i_z$.
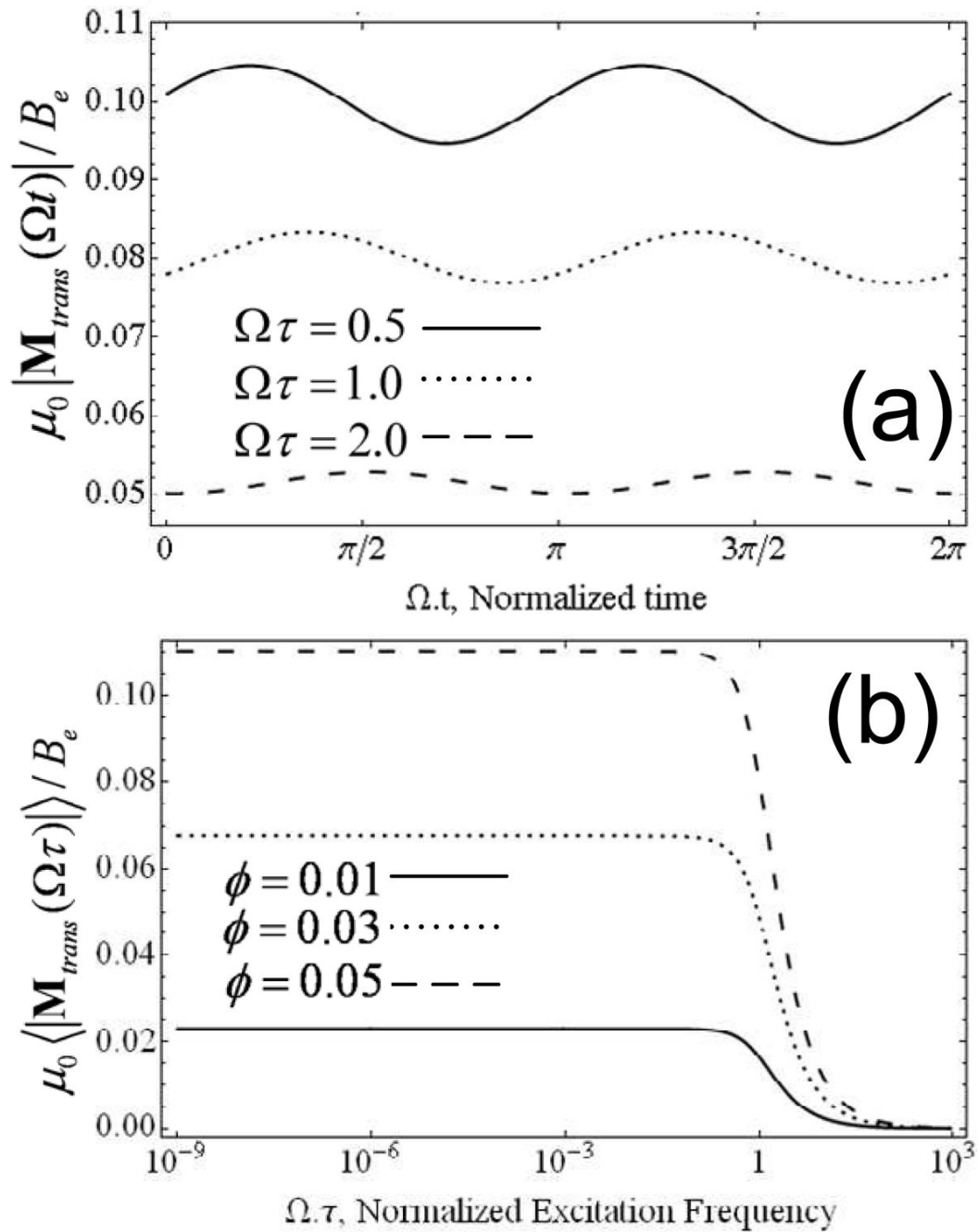
Fig. 4.
Time dependence of the transverse magnetization magnitude (a) for various values of $\Omega\tau$ plotted versus normalized time, Ωt for $\varphi = 0.05$ and (b) frequency dependence of the time-average normalized transverse magnetization for various φ is presented in the presence of rotating field excitation and in the absence of any imposed fluid flow. The φ-dependence in (b) arises from the dependence of the saturation magnetization, $M_s = \varphi M_d$. The channel width is 5 mm in each case while $B_0 = 0.2$ T and $B_e = 5\%$ of B_0.
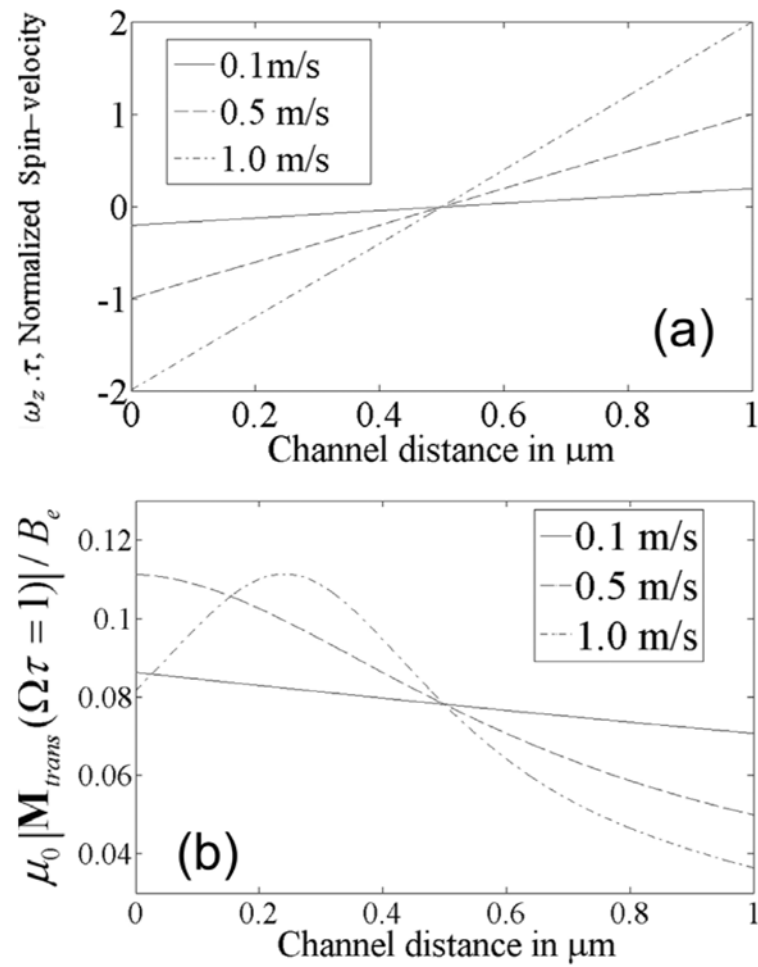
Fig. 5.
The normalized spin-velocity and the normalized, instantaneous, transverse magnetization are shown as a function of y, the channel width in μm for various maximum imposed Poiseuille flow velocities, U_p. $B_0 = 0.2$ T, $B_e = 5\%$ of B_0 and $\varphi = 3\%$. The channel width is $d = 1$ μm in each case and $\Omega\tau = 1$.

Table 1

Table of Nominal Physical Parameters

Symbol	Value	Quantity
B_0	0.2	Main Flux Density in T
H_0	B_0/μ_0	Main Field Intensity in water in A·m^{-1}
B_e	5% of B_0	Rotating Flux Density Amplitude in T
H_e	$B_e/\mu_0 = \hat{h}_x$	Rotating Field Intensity in water in A·m^{-1}
μ_0	$4\pi \times 10^{-7}$	Permeability of free space in H·m^{-1}
R	4×10^{-9}	Mean particle radius in m
V_p	$4/3\,\pi R^3$	Magnetic particle volume in m^3
φ	varied	Frequency of transverse $\boldsymbol{B}_e$ field rotation in Hz
Ω	$2\pi f$	Frequency of magnetic field rotation rad·s^{-1}
φ	0.03	Ferrofluid volume fraction of solids
α_0	$\frac{M_d V_p \mu_0 H_0}{kT}$	Equilibrium Langevin Parameter
M_0	$M_s L(\alpha_0)$	Equilibrium Ferrofluid Magnetization in A·m^{-1}
M_d	446×10^3	Single-domain magnetization (Fe$_3$O$_4$) in A·m^{-1}
M_s	φM_d	Ferrofluid saturation magnetization in A·m^{-1}
τ	10^{-6}	Ferrofluid Time Constant in s
η	0.00202	Ferrofluid Kinematic Viscosity in Pa·s [27] [28]
ζ	$1.5\,\eta\,\varphi\ for\ \varphi \ll 1$	Ferrofluid Vortex Viscosity in Pa·s [2]
T	295	Absolute temperature in K
k	1.381×10^{-23}	Boltzmann Constant in JK^{-1}
d	varied	Channel width in m
U_p	varied	Maximum flow velocity (Poiseuille flow) in m·s^{-1}